GEOPHONE NOISE ATTENUATION IN THE COMPLEX WAVELET DOMAIN FOR WAVEFIELD SEPARATION OF OCEAN BOTTOM SEISMIC DATA

HONG LIANG[1], HOUZHU ZHANG[1] and DONGLIANG ZHANG[2]

[1]*Aramco Americas: Aramco Research Ctr., 16300 Park Row, Houston, TX 77084, U.S.A. hong.liang@aramcoamericas.com*
[2] *EXPEC Advanced Research Center, Saudi Aramco, Dhahran 31311, Saudi Arabia.*

(Received September 30, 2021; revised version accepted May 25, 2022)

ABSTRACT

Liang, H., Zhang, H.Z. and Zhang, D.L., 2022. Geophone noise attenuation in the complex wavelet domain for wavefield separation of ocean bottom seismic data. *Journal of Seismic Exploration*, 31: 341-356.

For ocean bottom seismic data processing, hydrophone and vertical geophone are combined to separate wavefields into upgoing and downgoing components. However, vertical geophone usually records strong shear noise (also known as V_z noise), which can significantly contaminate the results of wavefield separation and degrade image quality. In this paper, we propose a workflow to attenuate geophone noise for wavefield separation of ocean bottom seismic data. The workflow includes three steps: (1) calibration of geophone data against hydrophone data; (2) combination of calibrated geophone and hydrophone data to perform initial decomposition of upgoing and downgoing waves; (3) using hydrophone data and the downgoing wavefields from initial decomposition to perform enhanced wavefield separation in the dual-tree complex wavelet domain. The enhanced wavefield separation is achieved by thresholding the amplitude ratio of the downgoing wavefields from initial decomposition and hydrophone data in the complex wavelet domain. The proposed method is demonstrated on both synthetic and field data.

KEY WORDS: wavefield separation, ocean bottom seismic, geophone noise, complex wavelet domain.

0963-0651/22/$5.00

INTRODUCTION

In ocean bottom cable and ocean bottom node acquisition, sensors containing both hydrophone and geophone are located on the sea floor. Geophones record directional particle motion, while hydrophones record omni-directional pressure. The upgoing waves exhibit the same polarity in hydrophone and vertical geophone data, while the downgoing waves shows opposite polarity in the two components. Hence, the two components are often combined (called dual sensor summation) to remove downgoing receiver-side ghosts through the process of wavefield separation (Barr, and Sanders, 1989; Ball and Corrigan, 1996; Soubaras, 1996).

One well-known challenge for the dual sensor summation of ocean bottom data is the geophone noise. This type of noise is strong in the vertical geophone component, and usually is very weak or not observed on the hydrophone component. It appears random on common shot gathers; however, it shows coherent converted wave moveout on common receiver gathers (Shatilo et al., 2004; Paffenholz et al., 2006b; Craft and Paffenholz, 2007). Paffenholz et al. (2006a, 2006b) showed that the geophone noise is a true measurement of the vertical movement of the ocean bottom. It could be caused by body waves converting to Stoneley waves due to scattering in the shallow seabed. Strong geophone noise can significantly deteriorate the dual sensor summation results. Therefore, geophone noise attenuation is required for further ocean bottom seismic data processing.

Many methods have been proposed to attenuate geophone noise by separating noise from signal using various criteria. Brittan and Starr (2003) described a technique to separate the signal from noise assuming that the signal fits a water layer reverberation model. Shatilo et al. (2004) proposed a velocity filtering method in the *f-k* domain by recognizing the moveout differences between signal and noise. The method proposed by Zabihi et al. (2011) calculates enhanced upgoing wavefields by rejecting noise from vertical geophone according to a derived signal coherency estimate. Poole et al. (2012) presented a method for geophone noise attenuation by thresholding the envelope ratio of the estimated downgoing wavefields to the hydrophone data in the τ-p domain. Jeong and Tsingas (2019) developed a geophone denoising workflow using four-component OBN data. Ren et al. (2020) proposed a method to attenuate geophone noise by thresholding the hydrophone/geophone amplitude ratio in the dual-tree complex wavelet domain.

Other methods attenuate geophone noise by matching the envelope of geophone to the hydrophone while preserving the phase information, utilizing the fact that the hydrophone component is hardly affected by geophone noise. Craft and Paffenholz (2007) presented a multi-dimensional envelope-based matching method in the local τ-p and time-frequency

domain for simultaneous geophone noise attenuation and wavefield separation. Yu et al. (2011) developed a local attribute matching method in the dual-tree complex wavelet domain.

Dual-tree complex wavelet transform has the properties of multiresolution, localization, and directionality (Selesnick et al., 2005; Yu et al., 2017), therefore, is an attractive multidimensional domain for seismic data processing. In this paper, we extend our previous work (Liang and Zhang, 2019) and propose a separation-based geophone denoising method in the dual-tree complex wavelet domain. The proposed method first performs geophone calibration and then attenuates geophone noise by thresholding the amplitude ratio of the downgoing wavefields from initial decomposition to hydrophone data in the complex wavelet domain. We use a synthetic example to compare the proposed method with two other methods that are also based on the dual-tree complex wavelet transform and present a field data example to demonstrate the effectiveness of this method.

THEORY

For dual sensor summation, geophone calibration is an important prerequisite, which is designed to remove any instrumental inconsistencies between the geophone and hydrophone (Soubaras, 1996; Melbø et al., 2002; Muijs et al., 2007). Brunellière et al. (2004) and Wang and Grion (2008) reviewed various calibration methods using different calibration windows. In this paper, we choose a window which contains mainly direct arrivals to derive the geophone calibration filter for the case of deep waters (Zabihi et al., 2011). Other calibration windows may be preferred in the case of shallow waters (Wang and Grion, 2008). In the window of direct arrivals, the direct arrival completely overlaps with the ocean bottom primary. The theoretical scalar that matches geophone data Z to hydrophone data P in this specific window will be the following (White, 1965; Liang and Zhang, 2019):

$$s = -\rho_0 v_0 \frac{1+K_r}{1-K_r} \quad , \tag{1}$$

where ρ_0 and v_0 are the density and velocity of water, respectively, and K_r is the seabed normal reflectivity.

Note that this scalar is the negative of the scalar derived by Barr and Sanders (1989). Therefore, upgoing waves are obtained by subtracting the calibrated geophone from hydrophone, and the downgoing waves are computed by summing the two. In order to calibrate both the amplitude and phase of the geophone, we use a filter f_c instead of a scalar (Soubaras, 1996) to calibrate geophone in the window containing mainly direct arrivals. The

calibration filter f_c is solved by minimizing the following cost function in the selected window:

$$\mathrm{E} = \sum \|P - f_c * Z\|^2 \quad , \tag{2}$$

where $*$ represents convolution in time domain.

We can obtain the upgoing wavefields U and downgoing wavefields D from initial decomposition as follows:

$$\mathrm{U} = \frac{P - f_c * \mathrm{Z}}{2} \quad , \tag{3}$$

changes to:

$$\mathrm{D} = \frac{P + f_c * \mathrm{Z}}{2} \quad . \tag{4}$$

Both U and D are contaminated by geophone noise. Similarly to Poole et al. (2012), we propose a method to first compute the amplitude ratio of D to P in the dual-tree complex wavelet domain, and then use thresholding to obtain an enhanced upgoing wavefield with geophone noise attenuated, utilizing the fact that a relatively large amplitude ratio indicates the existence of strong geophone noise.

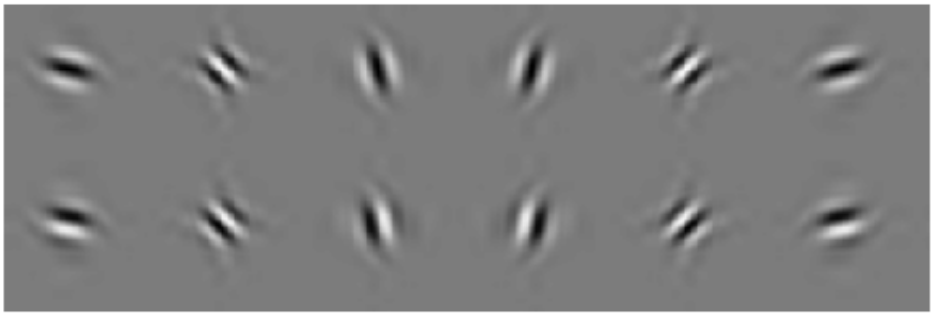

Fig. 1. The real (top) and the imaginary (bottom) part of the wavelet basis for the 2D complex dual-tree wavelet transform.

We choose the dual-tree complex wavelet transform to decomposes data into higher dimensions to better facilitate signal-noise separation. Compared to methods in *f-k* or *τ-p* domain, it is a local transform and will not spread out aliased energy in the seismic data (Yu et al., 2017). The 2D dual-tree complex wavelet transform recursively decomposes input data into four subbands: HH (high-f high- k subband), HL, LH, and LL subbands (Selesnick et al., 2005). This transform has wavelets oriented in six distinct

directions (±75°, ±45°, ±15°), as shown in Fig. 1. More details about the geophysical application of the dual-tree complex wavelet transform can be found in Yu et al. (2017). The 2D dual-tree complex wavelet transform of input data $d(t,x)$ can be represented as follows:

$$\tilde{d}(t,x,s,o,i) = CWT_{2D}\big(d(t,x)\big) \quad , \tag{5}$$

where s represents scale, o represents orientation, $i = real, imag$ indicates a real or imaginary part. Each orientation at a certain scale represents a dipping component at that frequency band.

The proposed workflow is as follows:

1. Apply the 2D dual-tree complex wavelet transform to both P and D.
2. Compute sample by sample amplitude ratio r of $\widetilde{D}/\widetilde{P}$ in the complex wavelet domain

$$r = \frac{\sqrt{\widetilde{D}(t,x,s,o,real)^2 + \widetilde{D}(t,x,s,o,imag)^2}}{\sqrt{\tilde{P}(t,x,s,o,real)^2 + \tilde{P}(t,x,s,o,imag)^2}}. \tag{6}$$

3. Assuming that noise and signal are separated in the multi-dimensional complex wavelet domain, the amplitude ratio would be extremely large in noise-dominant regions. Threshold the amplitude ratio r and obtain the enhanced upgoing wavefields in eq. (7):

$$\widetilde{U}' = \begin{cases} \tilde{P} - \widetilde{D}, & r \le \sigma_H \\ 0, & r > \sigma_H \end{cases}, \tag{7}$$

4. Compute the enhanced upgoing wavefields U' by applying an inverse complex wavelet transform to $\widetilde{U}'$. The enhanced downgoing wavefield can be obtained by subtracting U' from P.

NUMERICAL EXAMPLES

In this section, we will first compare the proposed method with two other methods that are also based on the dual-tree complex wavelet transform. The comparison is demonstrated on synthetic data. One field data example using the proposed method will also be presented.

Following Paffenholz et al. (2006b), we generate synthetic elastic models with random scatters inserted at the seafloor, as shown in Fig. 2. The spatial interval of the model grid for finite difference modeling is 2 m in

both vertical and horizontal directions. Figs. 2a and 2b show the P- and S-wave velocity models, respectively. The seafloor layer is a thin layer of 6 m with a background S-wave velocity of 110 m/s. The scatters are represented by random perturbations in the S-wave velocity at the seafloor, as shown in Fig. 2c. Fig. 3 shows common shot gathers of hydrophone and vertical geophone data, and Fig. 4 shows the corresponding data in common receiver gathers. Comparison of Figs. 3 and 4 illustrates the characteristics of geophone noise, i.e., random in the common shot gather while coherent in the common receiver gather, strong on geophone but very weak on hydrophone.

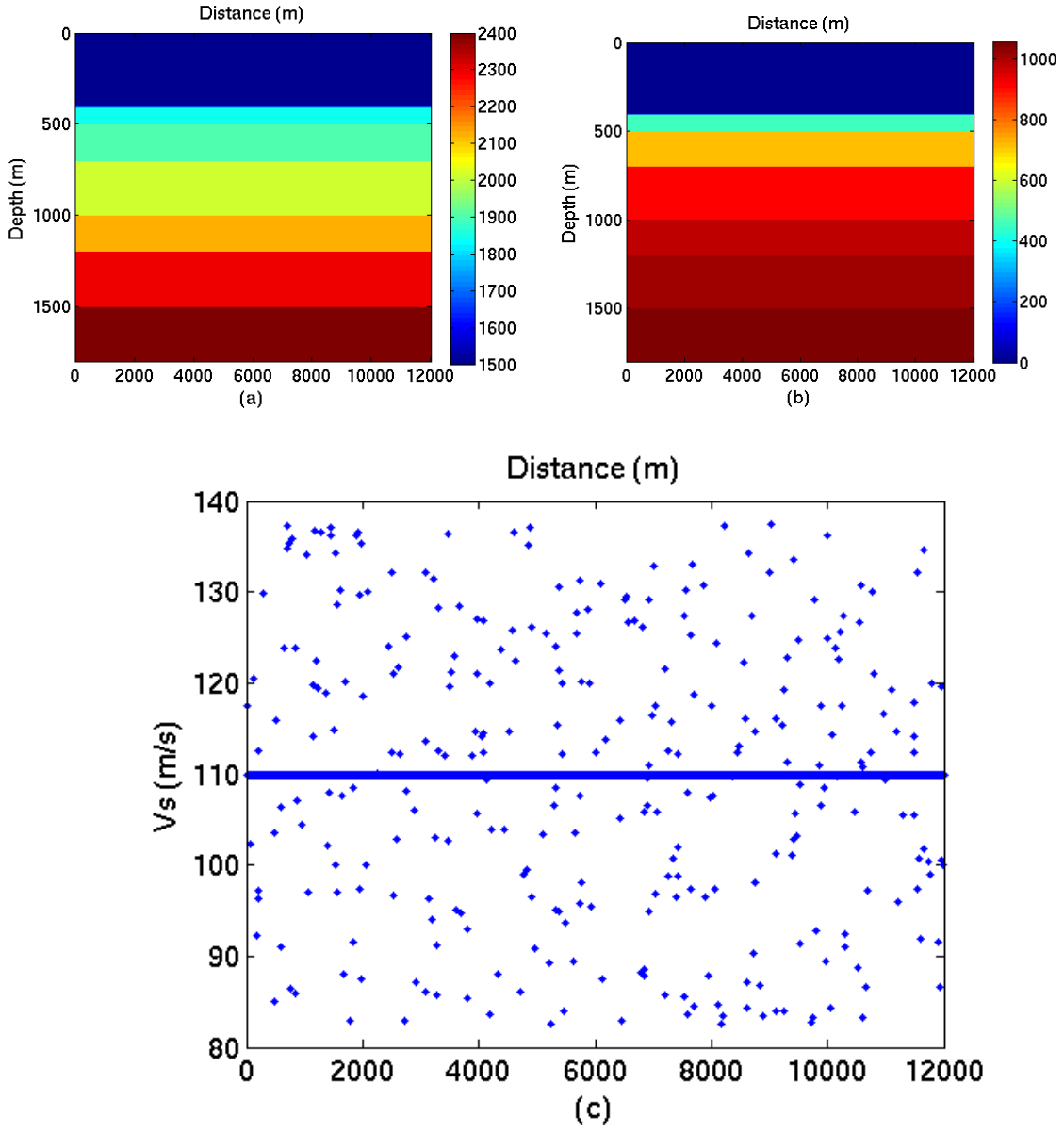

Fig. 2. Elastic finite difference models with random scatters at the seafloor: (a) V_p, (b) V_s, and (c) distribution of shear wave velocity at the sea floor.

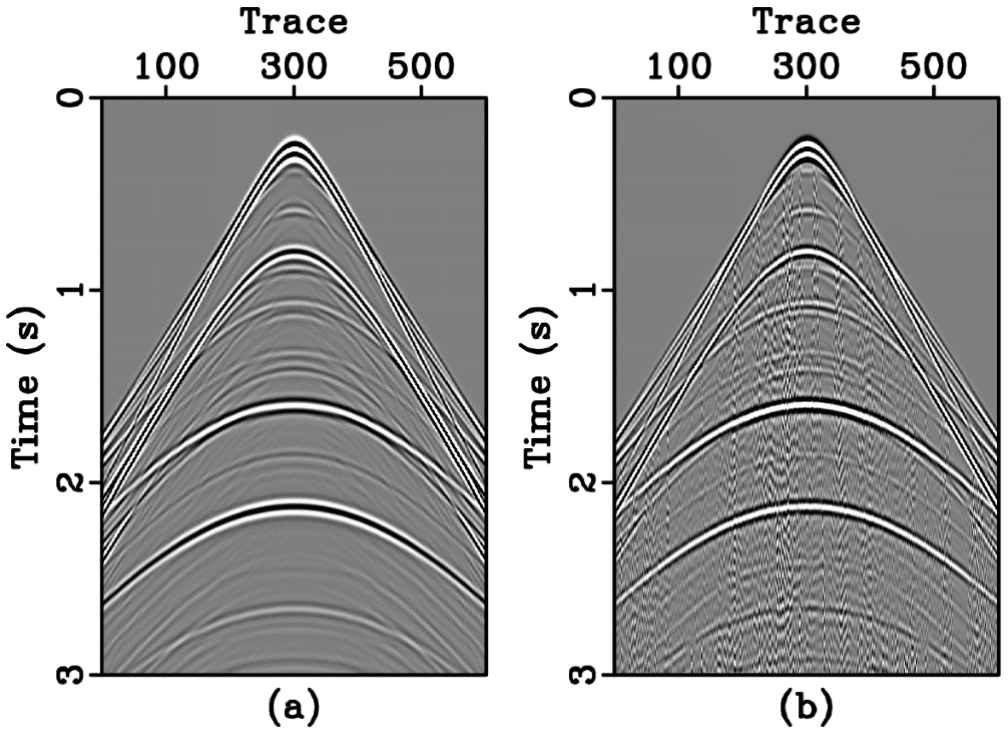

Fig. 3. Common shot gathers of hydrophone data (a) and geophone data (b).

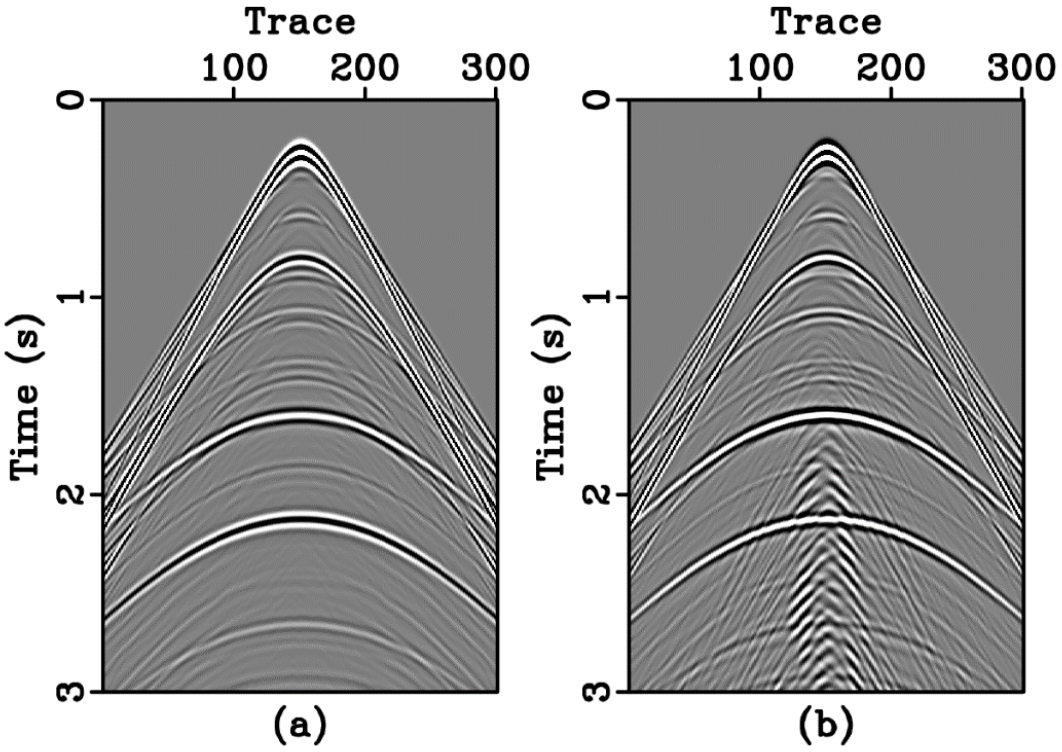

Fig. 4. Common receiver gathers of hydrophone data (a) and geophone data (b).

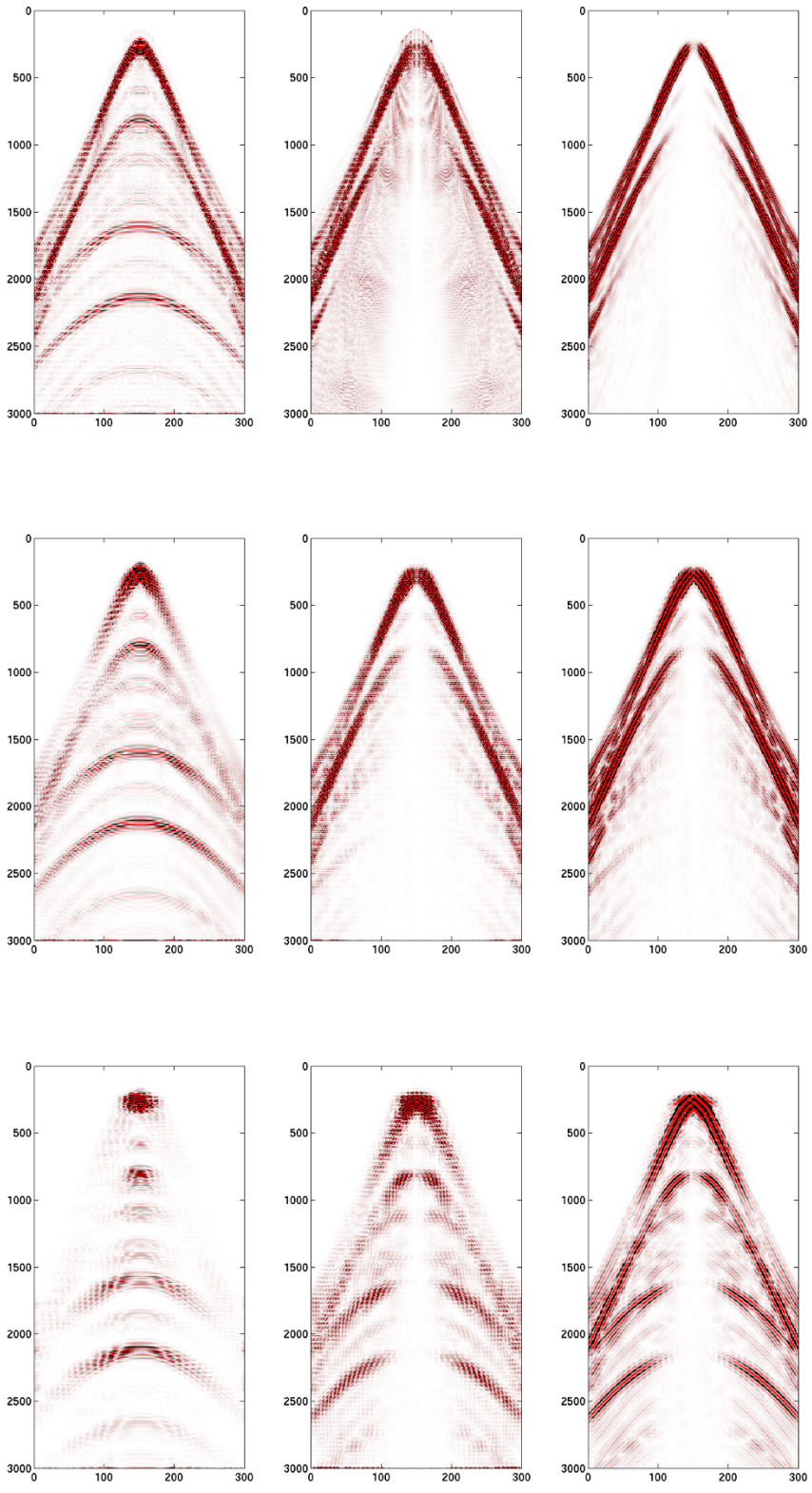

Fig. 5. Decomposition of P in the dual-tree complex wavelet domain.

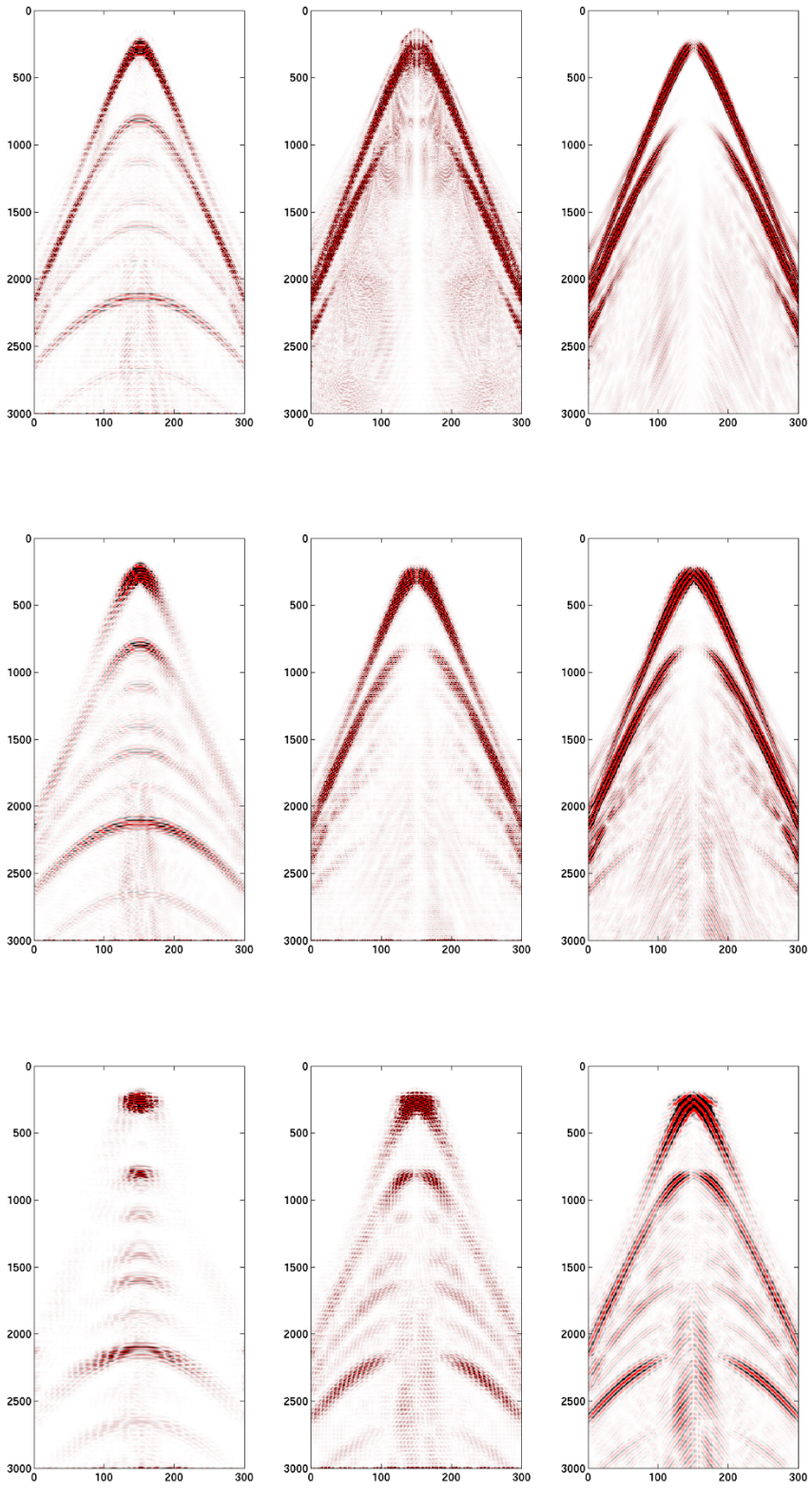

Fig. 6. Decomposition of D in the dual-tree complex wavelet domain.

Initial wavefield separation is performed using eqs. (3) and (4). We then apply the 2D dual-tree complex wavelet transform to P and D (with a total of 4 scales). Fig. 5 shows part of the decompositon of P in the complex wavelet domain. We combine negative and positive orientations, and the three colums from left to right in Fig. 5 show the decomposed wavefield in the following orientation: $o = \pm 15°, \pm 45°, \pm 75°$; the three rows from top to bottom represent three different scales: $s = 1,2,3$. Fig. 6 illustrates corresponding decomposition of D. Visual comparison between Figs. 5 and 6 shows the separation of signal and noise by the complex wavelet transform. For reference, Figs. 7a and 7b show the upgoing and downgoing wavefields from initial decomposition without denoising.

We first compare the proposed method with the method based on amplitude matching proposed by Yu et al. (2011). Both methods are implemented in the dual-tree complex wavelet domain. The method based on amplitude matching sets the amplitude of geophone to its hydrophone equivalent while preserving the phase information, thus, performs geophone denoising and wavefield separation in one step. Fig. 7c shows the results by using the method of amplitude matching of P and Z in complex wavelet domain, while Fig. 7d illustrates the upgoing wavefields using the proposed method of thresholding the amplitude ratio of $\widetilde{D}/\widetilde{P}$. The red ellipse in Fig. 7c highlights the residual noise in the separated upgoing wavefields, which is due to the fact that geophone noise also exisits in hydrophone data (can be weakly seen in Fig. 4a) and the amplitude matching can only scale down the noise. The amplitude ratio of $\widetilde{D}/\widetilde{P}$ is relatively large in this region since geophone noise is much weaker in the hydrophone than in geophone. Therefore, by rejecting noise according to the proposed method in eq. (7), less noise residual is seen in Fig. 7d. Also, when an upgoing event completely overlaps with an downgoing event with smaller amplitude, the method based on amplitude matching will remove both events in the separated upgoing wavefields. The yellow arrow in Fig. 7d points to an upgoing soure-side multiple that is removed in Fig. 7c but kept in Fig. 7d. This feature may not be desireable in some cases, for example, up/down deconvolution.

The amplitude ratio of geophone data Z to hydrophone data P can also be used to indicate strong geophone noise. Ren et al., (2020) proposed a method of hydrophone/geophone amplitude ratio thresholding to attenuate geophone noise. Next, we compare the two amplitude ratio thresholding methods. Fig. 8a shows the upgoing wavefield denoised by thresholding amplitude ratio of $\tilde{Z}/\tilde{P}$ in complex wavelet domain, and Fig. 8b shows the removed noise (i.e., difference between Figs. 7a and 8a). The obtained upgoging wavefields and the removed noise by the porposed method (thresholding amplitude ratio of $\widetilde{D}/\tilde{P}$) are shown in Figs. 8c and 8d, respectively. From the results we can see that using D and P instead of Z and

P can minimize the risk of damaging primaries since no primary energy is in the downgoing wavefields, as pointed out by Poole et al. (2012).

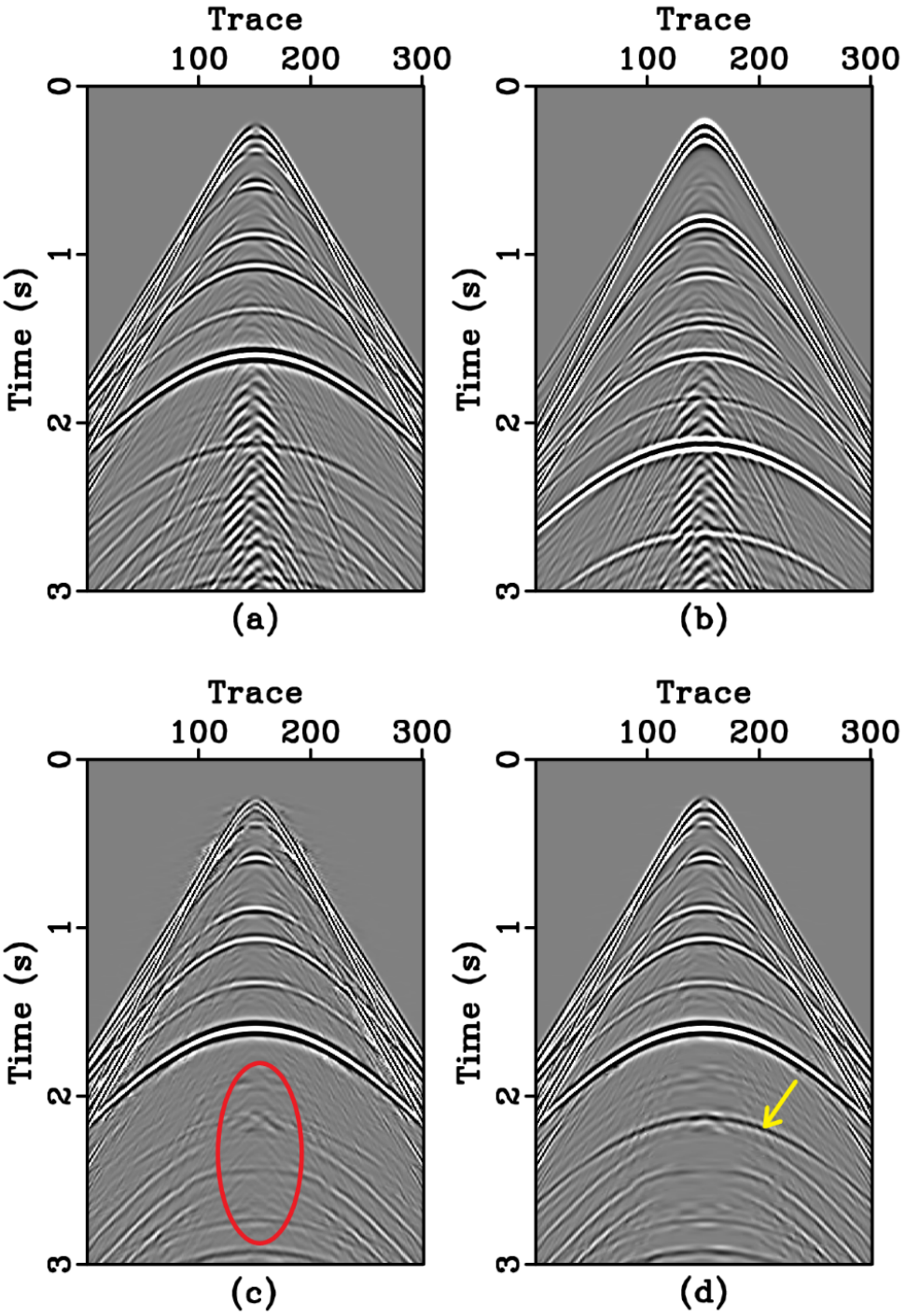

Fig. 7. Upgoing (a) and downgoing (b) wavefields without geophone denoising; upgoing wavefields denoised (c) using the method based on amplitude matching of *P* and *Z* in complex wavelet domain and (d) using the proposed method of amplitude thresholding.

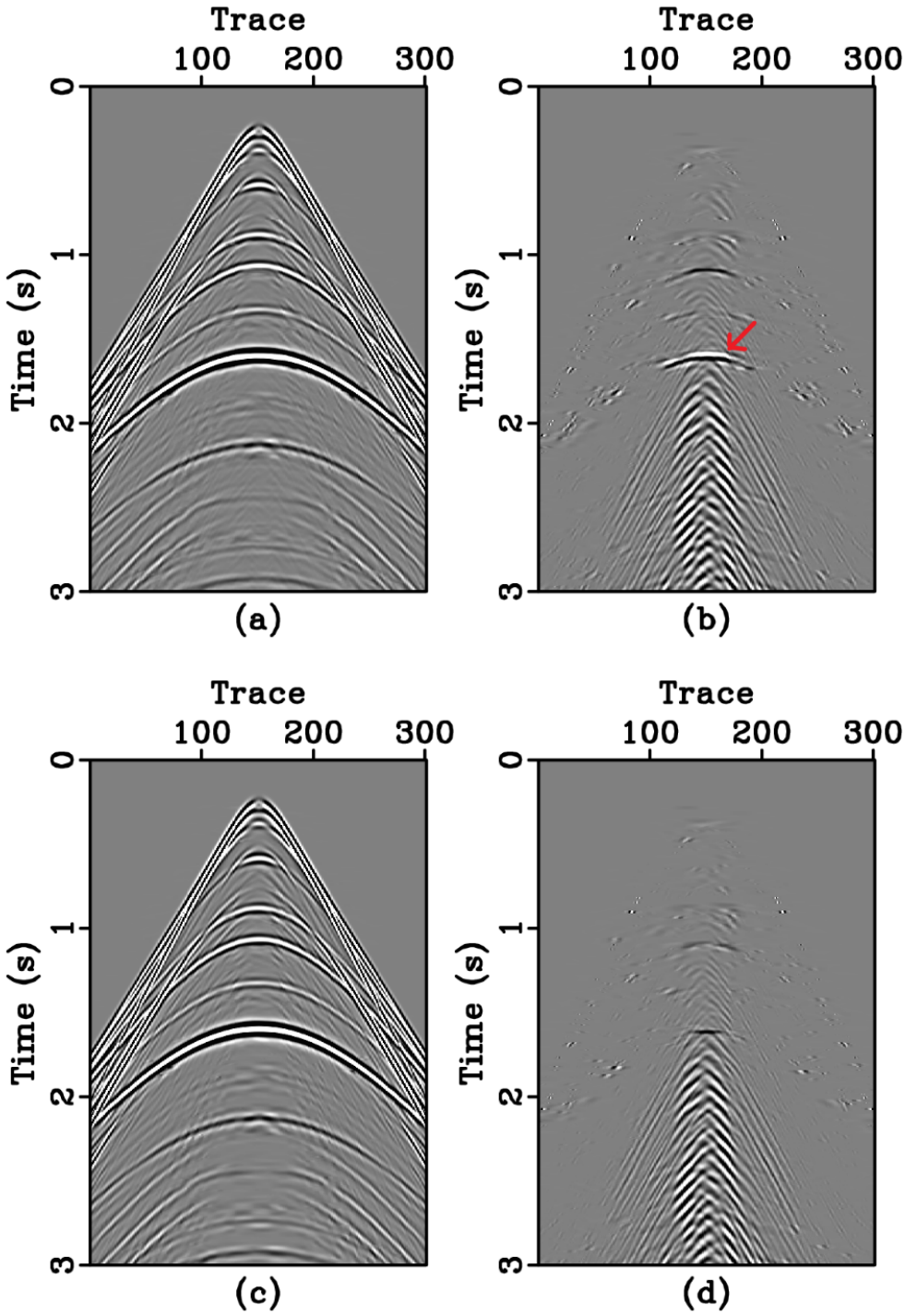

Fig. 8. (a) Upgoing wavefield denoised by thresholding amplitude ratio $\tilde{Z}/\tilde{P}$ in complex wavelet domain, and (b) removed noised in (a); (c) Upgoging wavefields denoised by using the porposed method (thresholding amplitude ratio of $\tilde{D}/\tilde{P}$) and (d) removed noise by the proposed method.

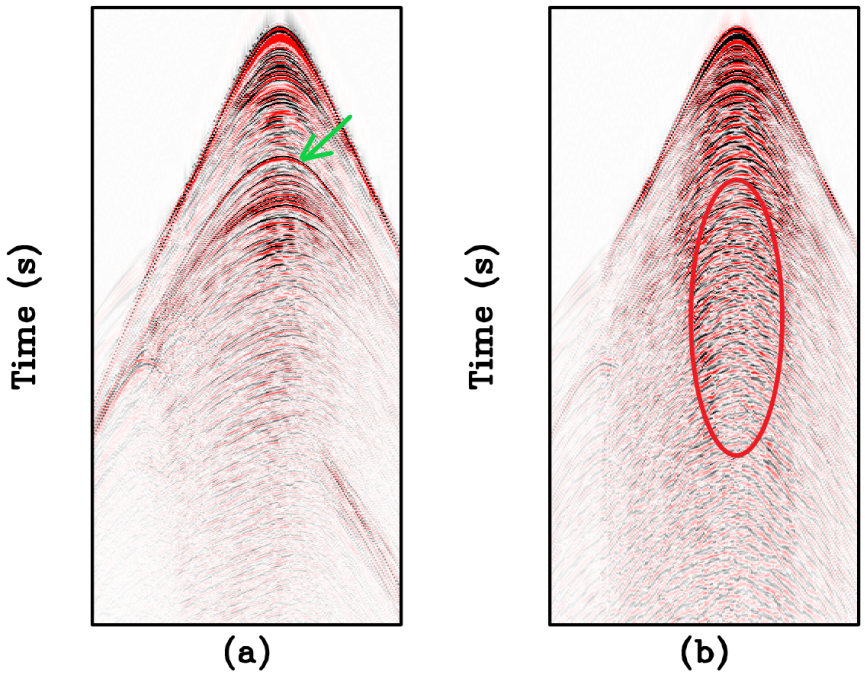

Fig. 9. Field data example: common receiver gathers of hydrophone (a) and geophone data (b).

Finally, we show an OBN field data example. Fig. 9 illustrates common receiver gathers of hydrophone (9a) and geophone data (9b). Geophone data exhibits strong geophone noise as indicated by the red ellipse in Fig. 9b. Figs. 10a and 10b show the upgoing and downgoing wavefields before denoising, respectively. We can see that the downgoing ghosts of direct arrivals (pointed by the green arrow in Fig. 9a) are removed from the upgoing component. However, both upgoing and downgoing waves are contaminated with strong geophone noise. The separated upgoing and downgoing wavefields look more like the geophone data. Figs. 10c and 10d show the corresponding components after denoising using the proposed method. Visually, events in the denoised upgoing and downgoing wavefields are more comparable to those in hydrophone data. Fig. 11 shows the FK spectra comparison of upgoing wavefields before and after denoising. We can see that the removed noises are mainly between 15 Hz and 30 Hz and mask some reflection events. Fig. 12 shows the receiver stack of hydrophone and geophone data. Strong geophone noise can clearly been seen in Fig. 12b. Figs. 13a shows the receiver stack of the upgoing wavefields from initial decomposition before denoising. The receiver stack of the denoised upgoing waves in Fig. 13b is much cleaner compared to Fig. 13a.

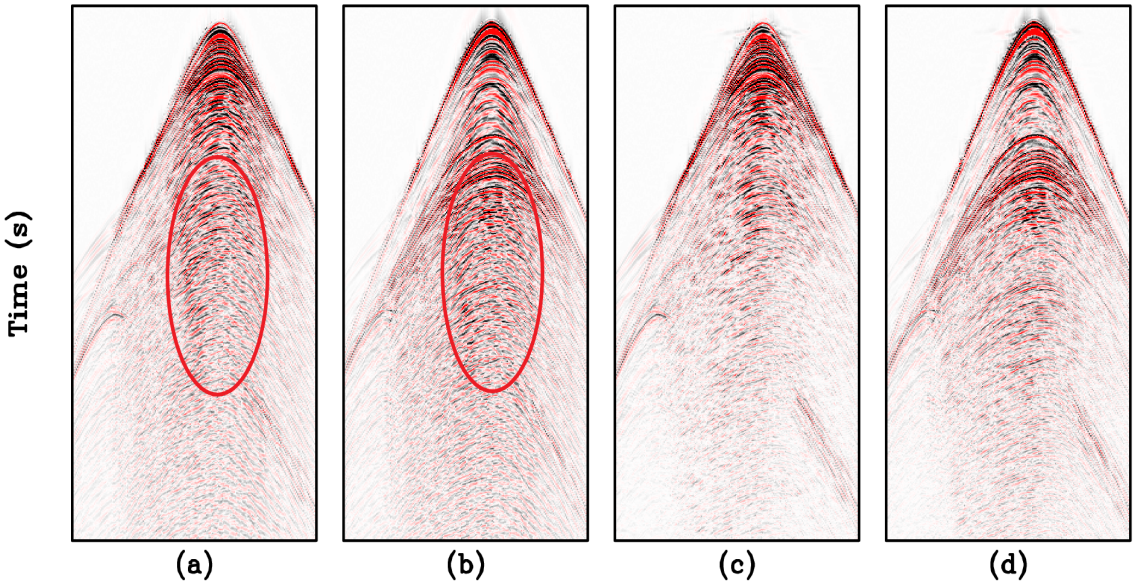

Fig. 10. Upgoing (a) and downgoing wavefield (b) before denoising; and upgoing (c) and downgoing (d) wavefield after denoising using the proposed method.

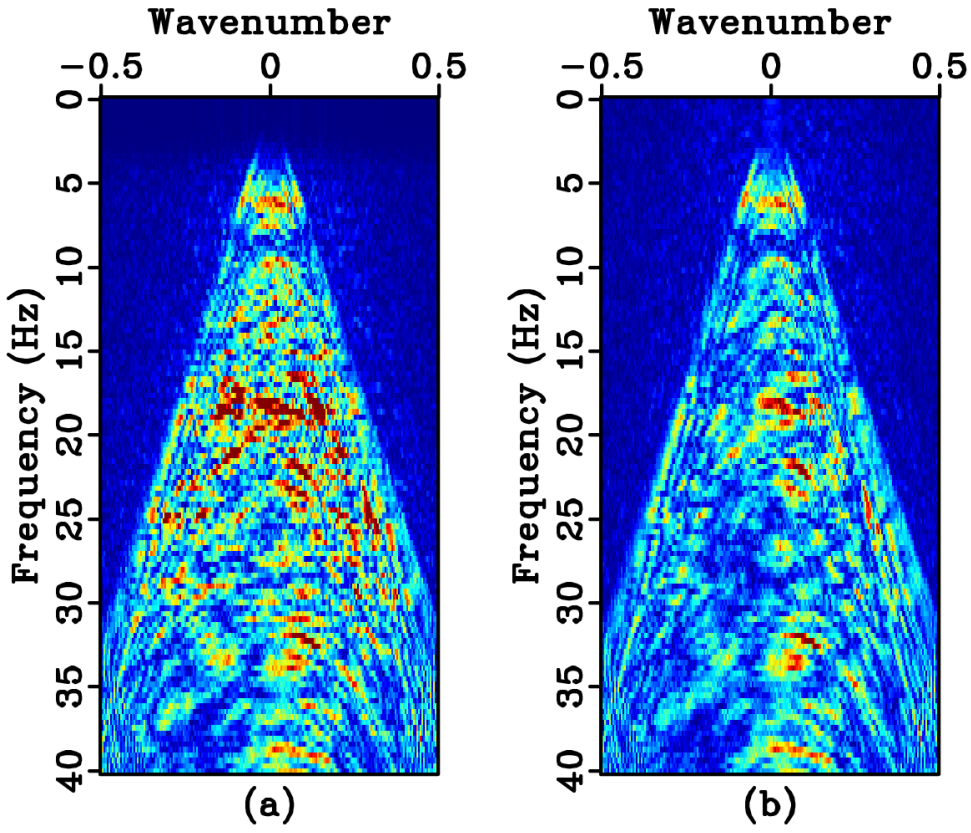

Fig. 11. FK spectra of upgoing wavefields before (a) and after (b) denoising.

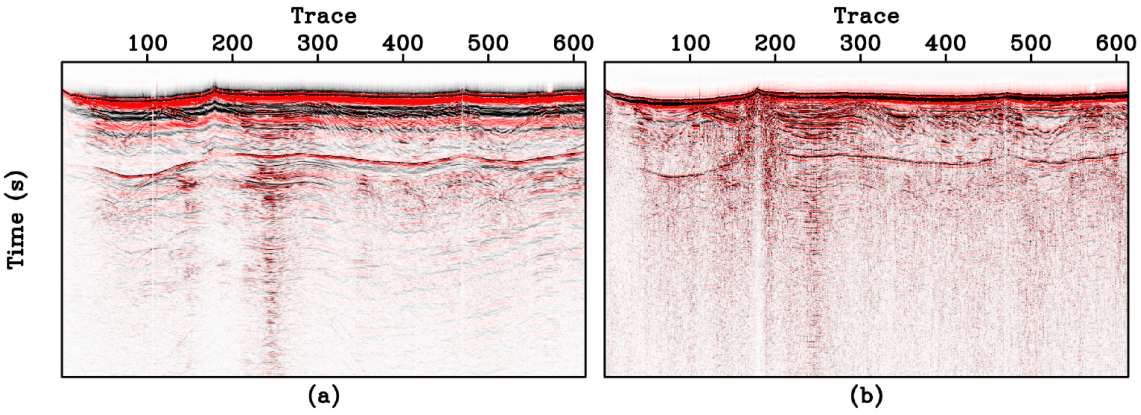

Fig. 12. Receiver stack of hydrophone (a) and geophone (b).

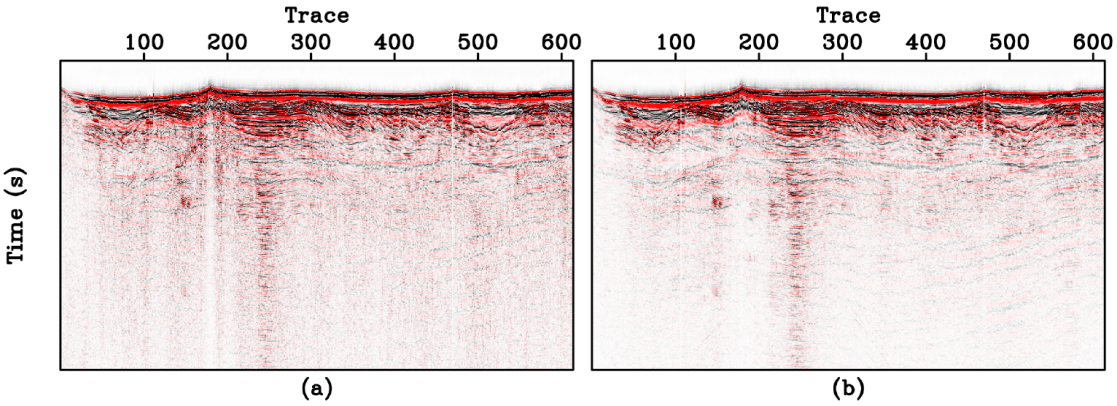

Fig. 13. Receiver stack of upgoing wavefield without denoising (a) and with denoising using the proposed method (b).

CONCLUSIONS

We have proposed a method to attenuate geophone noise for wavefield separation of ocean bottom seismic data. The enhanced wavefield separation is achieved by thresholding the amplitude ratio of downgoing wavefields and geophone data in the dual-tree complex wavelet domain. We compared the proposed method with the amplitude matching method and the geophone/hydrophone amplitude ratio thresholding method. The proposed method is demonstrated on both synthetic and field data example.

ACKNOWLEDGEMENTS

We would like to thank Cristina Young for her careful review of this paper.

REFERENCES

Ball, V. and Corrigan, D., 1996. Dual-sensor summation of noisy ocean-bottom data. Expanded Abstr., 66th Ann. Internat. SEG Mtg., Denver: 28-31.

Barr, F.J. and Sanders, J.I., 1989. Attenuation of water-column reverberations using pressure and velocity detectors in a water-bottom cable. Expanded Abstr., 59th Ann. Internat. SEG Mtg., Dallas: 653-656.

Brittan, J. and Starr, J., 2003. Applications of adaptive noise attenuation to dual sensor seismic data. Expanded Abstr., 73rd Ann. Internat. SEG Mtg., Dallas: 865-868.

Brunellière, J., Caprioli, P., Grion, S., Tilling, D., Amundsen, L. and Aronsen, H., 2004. Surface multiple attenuation by up-down wavefield deconvolution: An OBC case study. Expanded Abstr., 74th Ann. Internat. SEG Meeting, Calgary, Alberta: 849-852.

Craft, K., and Paffenholz, J., 2007. Geophone noise attenuation and wavefield separation using multidimensional decomposition technique. Expanded Abstr., 77th Ann. Internat. SEG Mtg., San Antonio: 2630-2634.

Jeong, W. and Tsingas, C., 2019. A de-noising methodology for multi-component seafloor nodal geophones. Extended Abstr.,81st EAGE Conf., London: 1-5.

Liang, H. and Zhang, H., 2019. Geophone noise attenuation after dual sensor summation for ocean bottom data in the wavelet domain, Geoconvention, Extended Abstr., 1-4.

Melbø, A.H.S., Robertsson, J.O. and van Manen, D.J., 2002. PZ calibration by applying the equation of motion to critically refracted waves. Expanded Abstr., 72nd Ann. Internat. SEG Mtg., Salt Lake City: 1030-1033.

Muijs, R., Robertsson, J.O. and Holliger, K., 2007. Data-driven adaptive decomposition of multicomponent seabed recordings: Application to shallow-water data from the North Sea. Geophysics, 69(5): 1329-1337.

Paffenholz, J., Shurtleff, R., Hays, D. and Docherty, P., 2006b. Shear wave noise on OBS Vz data - Part I, Evidence from the field. Extended Abstr., 68th EAGE Conf., Vienna: B046.

Paffenholz, J., Docherty, P., Shurtleff, R. and Hays, D., 2006a. Shear wave noise on OBS Vz data - Part II, Elastic Modeling of Scatterers in the Seabed. Extended Abstr., 68th EAGE Conf., Vienna: B047.

Poole, G., Casasanta, L. and Grion, S., 2012. Sparse t-p Z-noise attenuation for ocean-bottom data. Expanded Abstr., 82nd Ann. Internat. SEG Mtg., Las Vegas: 1-5.

Ren, Y., Yang, C., Degel, T. and Liu, Z., 2020. Vz noise attenuation using dual-tree complex wavelet transform. Expanded Abstr., 90th Ann. Internat. SEG Mtg., Houston: 1830-1834.

Selesnick, I.W., Baraniuk, R.G. and Kingsbury, N.C., 2005. The dual-tree complex wavelet transform. IEEE Sign. Process. Magaz., 22(6): 123-151.

Shatilo, A., Duren, R. and Rape, T., 2004. Effect of noise suppression on quality of 2C OBC image. Expanded Abstr., 74th Ann. Internat. SEG Mtg., Denver: 917-920.

Soubaras, R., 1996. Ocean bottom hydrophone and geophone processing. Expanded Abstr., 66th Ann. Internat. SEG Mtg., Denver: 24-27.

Wang, Y. and Grion, S., 2008. PZ calibration in shallow waters: the Britannia OBS example. Expanded Abstr., 78th Ann. Internat. SEG Mtg., Las Vegas: 1088-1092.

White, J.E., 1965. Seismic Wave Radiation. Geophysical Projection., 33: 956-969. Transmission and Attenuation. McGraw-Hill Book Company, New York.

Yu, Z., Kumar, C. and Ahmed, I., 2011. Ocean bottom seismic noise attenuation using local attribute matching filter. Expanded Abstr., 81st Ann. Internat. SEG Mtg., San Antonio: 3586–3590.

Yu, Z., Abma, R., Etgen, J. and Sullivan, C., 2017. Attenuation of noise and simultaneous source interference using wavelet denoising. Geophysics, 82(3): V179-V190.

Zabihi, E., Baboulaz, L. and Grion, S., 2011. Enhanced wavefield separation of OBS data. Extended Abstr., 73rd EAGE Conf., Vienna: CP-238.